ORIGINAL ARTICLE

Erosion Wear Behavior of High Chromium Cast Irons

Bratislav M. Rajicic[1] [ORCID] **· A. Maslarevic[2] · G. M. Bakic[2] ·
V. Maksimovic[3] · M. B. Djukic[2]**

Abstract In this study, two high chromium cast irons
(HCCI) with different chromium content (15%Cr and
25%Cr), in as-cast and annealed conditions (heat-treated,
HT), were tested to determine the erosion wear behavior of
these alloys. Erosion tests were done using a gas blast sand
facility with high erodent particle velocity (90 m/s) and high
erodent feed rate, at an impact angle of 45°, which represents
conditions similar to service conditions of some components
of thermal power plants using pulverized high mineral con-
tent coals. To identify erosion mechanisms, microstructural
characterization was done by a scanning electron microscope
on samples before and after erosion tests. Identification of
microstructural phases was done by X-ray diffraction analy-
sis. The main results of the tests shown in this paper indicate
that matrix plastic deformation and distribution of carbide
phase have a significant contribution to erosion resistance of
HCCI alloys in severe erosion service conditions.

✉ Bratislav M. Rajicic
brajicic@mas.bg.ac.rs

1 Innovation Center, Faculty of Mechanical Engineering,
University of Belgrade, Kraljice Marije 16, 11120 Belgrade,
Serbia

2 Faculty of Mechanical Engineering, University of Belgrade,
Kraljice Marije 16, 11120 Belgrade, Serbia

3 Vinca Institute of Nuclear Sciences, National Institute
of the Republic of Serbia, University of Belgrade,
11001 Belgrade, Serbia

1 Introduction

Erosion wear of materials is caused by the relative move-
ment of solid particles and the surfaces of components. Such
erosive wear can lead to the failure of industrial components
in a very short time and/or a sharp decline in the structural
integrity of industrial equipment. One example is severe ero-
sive/abrasive wear of pulverized coal thermal power plant
(TPP) components caused by ash with high mineral content
[1]. In this regard, any improvement in the erosion resist-
ance of materials represents a significant improvement in the
extension of the service life of such components [2].

The materials used in this erosion wear behavior study
are high chromium cast irons (HCCI), and well-known com-
mercial alloys used in industrial plants exposed to severe
erosive/abrasive wear conditions are present. These alloys
showed very high resistance to erosion mainly due to the
presence of hard eutectic carbides in the matrix [3, 4]. The
erosion wear behavior of high chromium cast irons with
various Cr content and microstructure is extensively stud-
ied but mostly using much lower erodent particle velocity
than in this study (90 m/s) [5–8]. The solid particle erosion
behavior of HCCI alloys strongly depends on the applied
heat treatment, obtained size and distribution of secondary
carbides, erodent impingement angles, and the type of pow-
der used for the erosion test [6, 7]. These parameters also
define the general materials loss and the various dominant
erosion wear morphologies and mechanisms of HCCI alloys
[7, 8]. It seems that in order to define optimal heat treatment
to improve erosion wear behavior of HCCI needs compre-
hensive investigations of the effect of heat treatments on
the microstructure, distribution and amount of primary and
secondary carbides, toughness, hardness, and finally, erosion
wear resistance of various HCCI [8].

The difference in erosion resistance of ductile and brittle materials is most pronounced from the aspect of mass loss at a different impact angle of erodent particles during erosive wear. The highest mass loss for brittle materials is obtained at the impact angles of erodent particles close to 90° [9, 10]. Contrary, the maximum mass loss for typically ductile materials is observed at approximately 45° impact angle [11]. The erosive wear is most affected by material hardness, as well as (1) type of fluid (density and ambient pressure, corrosivity, temperature, etc.) [12–14]; (2) type of erodent (density, shape, size, and hardness); (3) fluid flow (impact angle, particle velocity, and kinetic energy) [15, 16]; and (4) material properties (fracture toughness, residual stress, microstructure, and surface roughness/treatment) [3, 4, 11, 17].

Fe–Cr-C alloys have superior erosion/abrasion wear resistance in severe operating conditions [18]. Several types of carbides are present in the Fe–Cr–C alloys, such as $(Fe,Cr)_3C$, $(Fe,Cr)_7C_3$, $(Fe,Cr)_{23}C_6$, and $(Fe,Cr)_3C_2$ [3, 19]. As the chromium (Cr) content increases, the type of eutectic carbide in Fe–Cr–C alloys changes from M_3C to M_7C_3 type [4]. Eutectic carbides of M_3C type are present in unalloyed or alloyed white cast irons with lower Cr content ($<5\%$) and up to 2% C, while with the increase of chromium content up to 8–10%, eutectic carbides become less continuous and fracture toughness improves [3]. The form of eutectic carbides changes to discontinuous type M_7C_3 with $Cr > 10\%$, while for $Cr > 30\%$ chromium carbides of the $(Cr, Fe)_{23}C_6$ type typically appears [4, 20].

The aim of this paper is to study the erosive wear resistance of two HCCI alloys with different chemical compositions in the as-cast and heat-treated conditions, after an erosion test with a high erodent particle velocity (90 m/s) and high feed rate (3000 g/min) of solid eroding particles.

Table 1 Heat treatment (HT) parameters

Heating temp. (°C)	Heating rate (°C/h)	Holding time (h)	Furnace cooling (h)
600	60	1	-
600–960	60	2	48

Table 3 Erosion test parameters

Parameter	Value
Type of erodent	Foundry quartz sand
SiO_2 content(wt.%)	min 98.0
Mean erodent granulation (mm)	0.26
Feed particle rate (g/min)	3000
Impact velocity − mean value (m/s)	90
Erodent particles impact angle (°)	45
Nozzle diameter (mm)	9
Distance between nozzle and sample (mm)	370
Erosion test duration (s)	600
Carrying gas	Air
Temperature (°C)	22

2 Experimental Methods

2.1 Material and Procedure

The samples used in this experiment were made by sand casting. Melting of metal was performed in an induction furnace "Inductotherm" 500 kV, capacity 1000 kg/h. A molding mixture of sand and binder resins was used for the production of sand molds, with a casting temperature of 1460–1520 °C. The dimensions of the samples were $\sim 120 \times 120 \times 10$mm, and the weight of the samples was approximately 1100 g.

Testing samples were made of two HCCI alloys, with different Cr content, 15%Cr and 25%Cr. Two samples were made from each HCCI alloy in order to test and compare the erosion wear behavior of the alloy in the as-cast and heat-treated (HT) conditions (annealing in 300 KW furnace; up to 1200 °C). The parameters of multi-step heat treatment are shown in Table 1.

Analysis of the chemical composition of both HCCI alloys was performed after HT on the Thermo Fisher Scientific Optical Emission Spectrometer, type ARL iSpark 8820 Package FE2. As shown in Table 2, the first HCCI alloy is 15%Cr type (HCCI-15), while the second is 25%Cr type (HCCI-25).

X-ray diffraction (XRD) analysis of both samples was performed using a Rigaku Ultima IV diffractometer, CuKα radiation ($\lambda = 1.540598$ Å). The scanning of samples was done through a range of 2θ diffraction angles (30°–100°), with a step size of 0.02°. Phase identification of the data

Table 2 Chemical composition of alloys after HT

	Element (wt%)						
	C	Mn	Si	Ni	Cr	Mo	Rest
HCCI-15	2.30	0.79	0.73	0.88	14.30	1.43	Residue
HCCI-25	3.00	0.45	0.44	0.59	24.40	0.21	Residue

Fig.1 Solid particle erosion test installation: 1—Air compressor with pressure regulator, 2—flow meter, 3—mixing chamber with particle tank, 4—nozzle
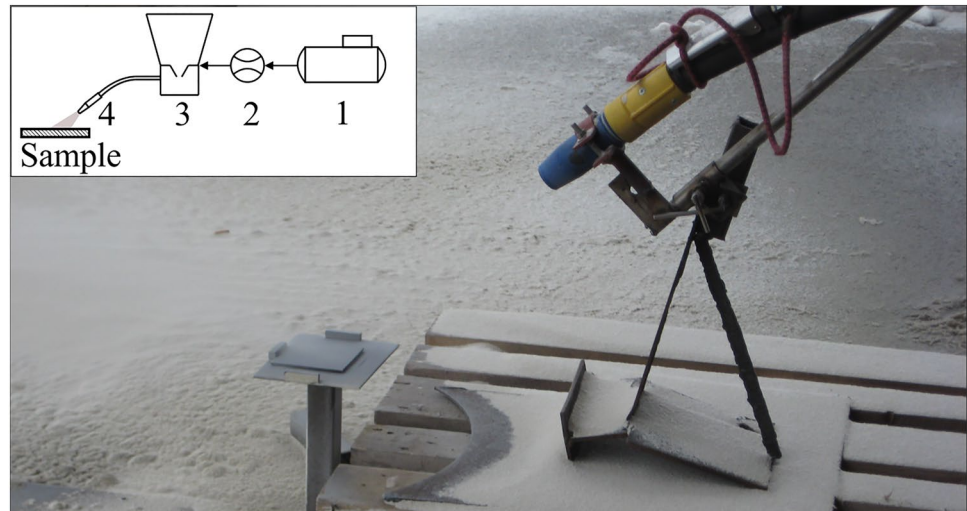

collected was performed by the program DIFFRACplus using the database for XRD peak identification compiled by the Joint Committee on Powder Diffraction Standards (JCPDS).

Metallographic characterization of both HCCI alloy samples, as-cast and after HT, was carried out by field-emission scanning electron microscope (FE-SEM), TESCAN Mira3 XMU type, operating at 20 kV at different magnifications. Cutting, grinding, polishing, and etching (Vilella's reagent 5 ml HCl + 2 g Picric acid + 100 ml Ethyl alcohol) was done as a standard preparation procedure for SEM specimens.

Also, hardness measurements were performed on the cross-section of all samples using the Rockwell TO 5006 device, and the mean values are presented in this paper.
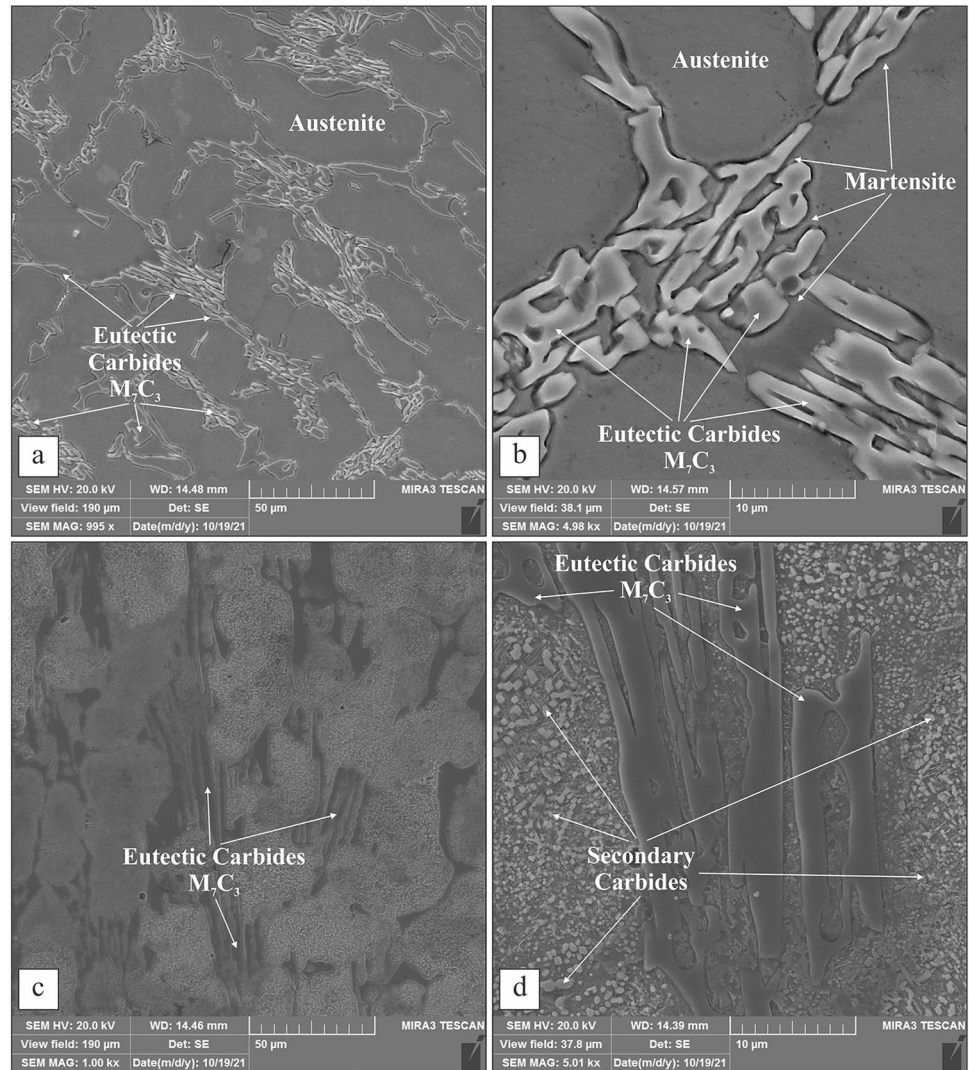
2.2 Erosion Test

One of the commonly used tests for characterizing the erosion properties of materials is the "Erosion Tests by Solid Particle Impingement Using Gas Jets" according to ASTM G76 [21]. However, the erodent particle velocity in this test is too small compared to the actual service conditions of TPP components exposed to severe erosion with a very high feed rate of erosive particles [22]. The selected high erodent particle velocity (90 m/s) in this study is much higher than those recommended in the ASTM G76-07 standard. Previously published studies highlighted the necessity of erosion resistance testing of industrial components, mostly in TPP [22], exposed to severe erosion conditions using high-velocity particles (~ 100 m/s) [2, 15, 23, 24], more than three times higher than used per ASTM G76-07 standard.
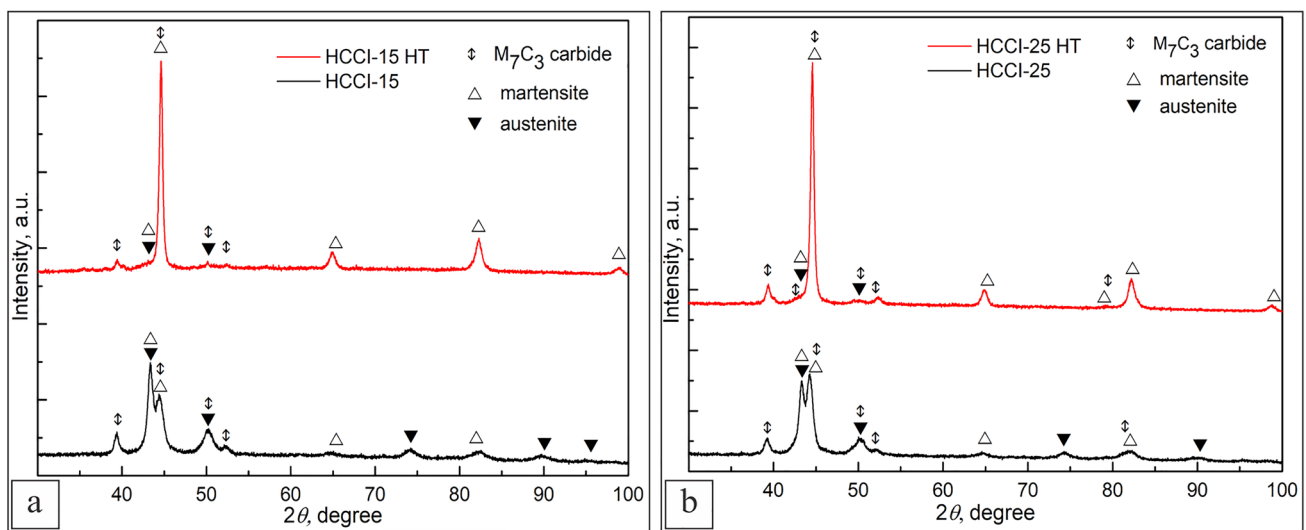
Fig. 2 XRD patterns of samples: **a** HCCI-15 (as-cast and after HT), **b** HCCI-25 (as-cast and after HT)

Fig. 3 SEM micrographs of HCCI-15 samples: as-cast (**a**, **b**) and after HT (**c**, **d**)

Therefore, in this study, the erosion test was modified in such a way that the impact velocity of solid erodent particles was significantly higher, i.e., 90 m/s compared to the standard 30 m/s, and also with a very high feed rate, i.e., a higher concentration of erodent particles, approximately 3000 g/min (compared to the standard 2 g/min). The impact angle of solid eroding particles was 45°. The erosion test parameters are shown in Table 3.

A specially designed installation was used for the gas blast sand erosion test, as shown in Fig. 1. Other authors have also used similar installations for erosion tests [25–27].

Two samples of both alloys (HCCI-15 and HCCI-25) were made, which makes a total of 4 samples that were tested for erosion. Two samples were tested in the as-cast condition (HCCI-15 and HCCI-25), and the remaining two were tested after the heat treatment (HCCI-15-HT and HCCI-25-HT). All 4 samples had the same dimensions (~ 120 × 120 × 10 mm, weight ~ 1100 g) and were tested
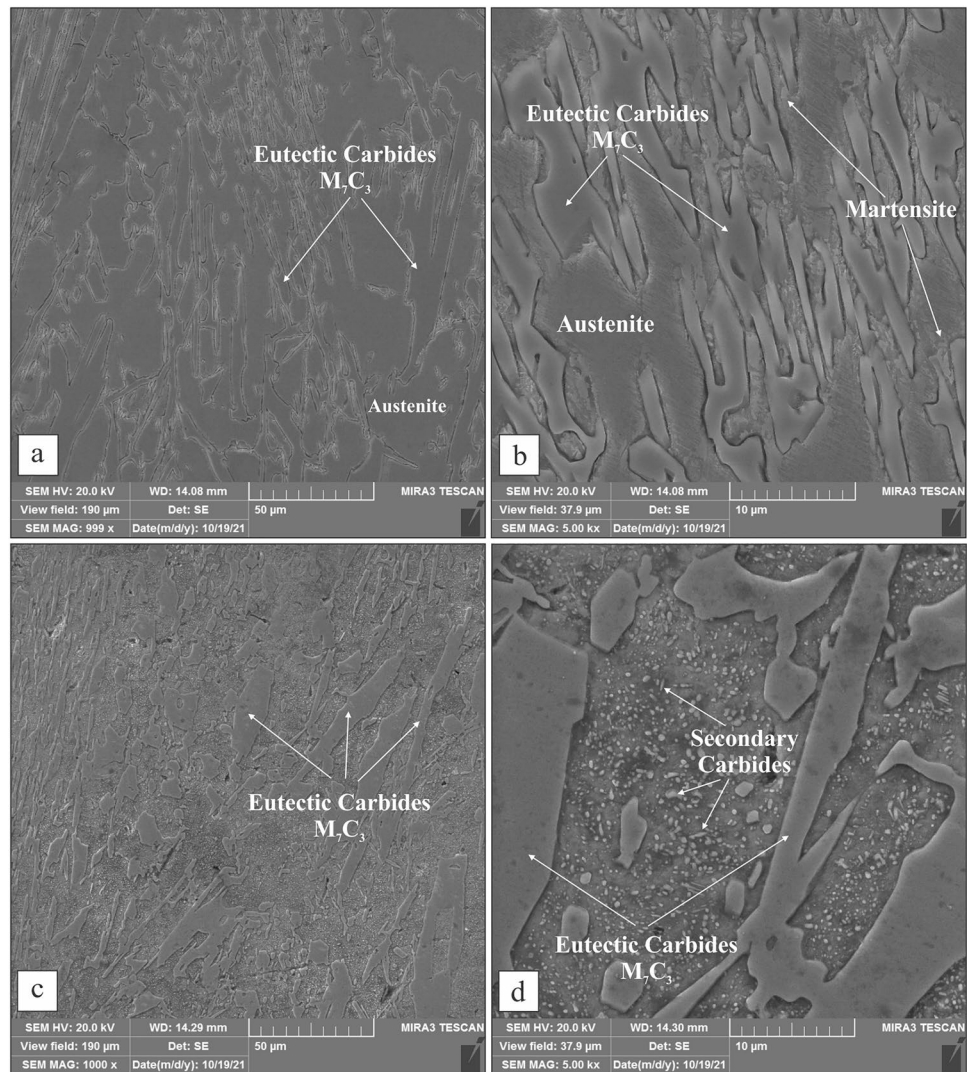
under the same conditions specified in Table 3. Based on the double disk method [28], a mean particle velocity of 90 m/s was calculated for this test. To determine the mass loss of eroded samples, the mass of the sample was measured before and after the erosion test. The mass of the samples was measured with an analytical weighing balance (Mettler Toledo type) with an accuracy of 0.1 g.

3 Results and Discussion

The eutectic composition of the HCCI alloys can be calculated using Eq. (1) [29, 30]:

$$[\%C] + 0.00474 \times [\% \, Cr] = 4.3 \tag{1}$$

Fig. 4 SEM micrographs of HCCI-25 samples: as-cast (**a**, **b**) and after HT (**c**, **d**)

	Rockwell hardness [HRC]
HCCI-15	44–46
HCCI-15-HT	30–32
HCCI-25	54–56
HCCI-25-HT	34–36

Table 4 Hardness of samples

where the result of the equation represents the theoretical value according to which the HCCI alloys are divided into hypoeutectic (< 4.3) or hypereutectic (> 4.3). Based on the chemical composition shown in Table 1 and according to the calculation results per Eq. (1), both tested alloys, HCCI-15 (% C = 2.98) and HCCI-25 (% C = 4.16), are of hypoeutectic type.

3.1 Microstructure of Samples

The X-ray diffraction patterns of HCCI-15 and HCCI-25 alloys, as-cast and after HT, are shown in Fig. 2a, b. They revealed the presence of M_7C_3 carbides, austenite, and martensite. In both samples, a decrease in the content of austenite in the material is observed after HT.

In the as-cast condition, the microstructure of the HCCI-15 and HCCI-25 samples consists of a two-phase matrix, i.e., austenitic-martensitic matrix and eutectic carbides, as shown in Figs. 3a, b and 4a, b. After the heat treatment, the microstructure for both alloys mainly consists of martensite and secondary carbides matrix, and eutectic carbides, as shown in Figs. 3c, d and 4c, d.

During the process of eutectic solidification of hypoeutectic white cast iron, the formation of austenitic dendrites occurs first [31, 32]. After that, when the temperature reaches the eutectic temperature, a eutectic reaction occurs which results in forming of a eutectic mixture of austenite

Fig. 5 Eroded HCCI samples, as-cast and HT: **a** HCCI-15, **b** HCCI-15-HT, **c** HCCI-25, **d** HCCI-25-HT
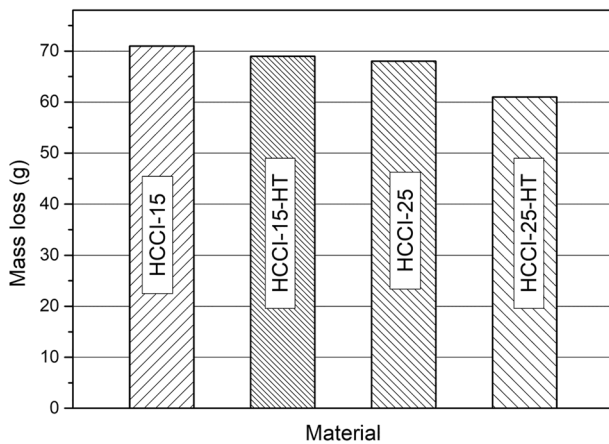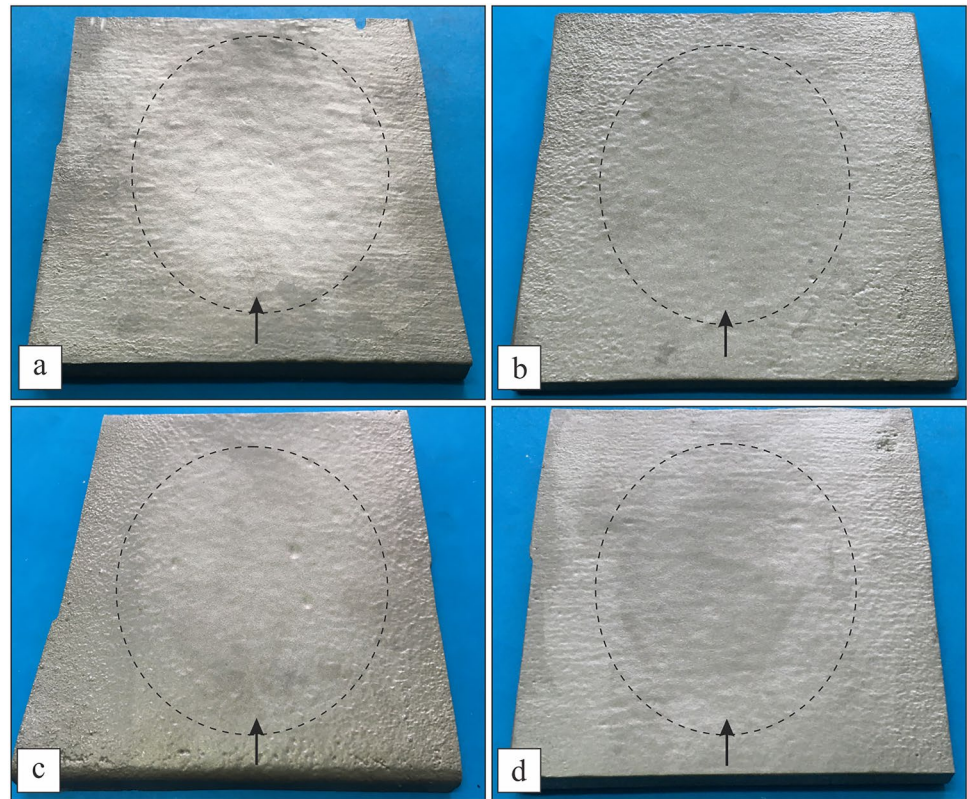
Fig. 6 Erosion test results—mass loss of different HCCI alloys (as-cast and after HT)

and carbide. Furthermore, eutectic carbides absorb C and alloying elements from austenite, so the narrow zone at the austenite/carbide boundary becomes depleted with alloying elements. Such a lack of C and alloying elements increases the temperature of the beginning of martensitic transformation (Ms), which leads to the transformation of austenite into martensite in these zones, as marked in Fig. 3b.

The solidification process of these types of alloys (Fe–Cr–C) with various Cr content was previously reported

[32–35]. The martensitic matrix of the HCCI-15 specimen is located in a narrow zone around eutectic carbides, and its content is significantly lower compared to the austenitic phase content, as shown in Fig. 3b. Also, austenite and martensite are identified in the HCCI-15 specimen, as shown in Fig. 2a. After annealing, the microstructure of the HCCI-15-HT sample has very fine secondary carbides distributed throughout the martensitic-austenitic matrix, in addition to eutectic carbides, as shown in Fig. 3c, d. Due to the high density of secondary carbides, it is very difficult to identify the matrix microstructure. The X-ray diffraction patterns of HCCI-15-HT show that the matrix is mostly martensitic with the remaining amount of residual austenite, as shown in Fig. 2a.

The microstructure of the HCCI-25 sample (as-cast condition), as shown in Fig. 4a, b, consists of the austenitic-martensitic matrix with eutectic carbides of M_7C_3 type, as shown in Fig. 2b. The martensitic zones in the HCCI-25 sample are wider in comparison with the HCCI-15 sample, as shown in Fig. 4a, b and Fig. 3a, b. After HT in the matrix, in addition to dendritic eutectic carbides, also primary carbides in the interdendritic places are present, as shown in Fig. 4d. Only M_7C_3 type of carbides is observed by XRD analyses.

The percentage of carbides in the samples in the as-cast condition can be determined according to the following empirical formula $\% K = 12.33 \times \text{wt.\%} \, (C) + 0.55 \times \text{wt.\%}$

Fig. 7 SEM micrographs of eroded surface morphology HCCI-15 alloys: as-cast (**a**, **b**) and after HT (**c**, **d**)
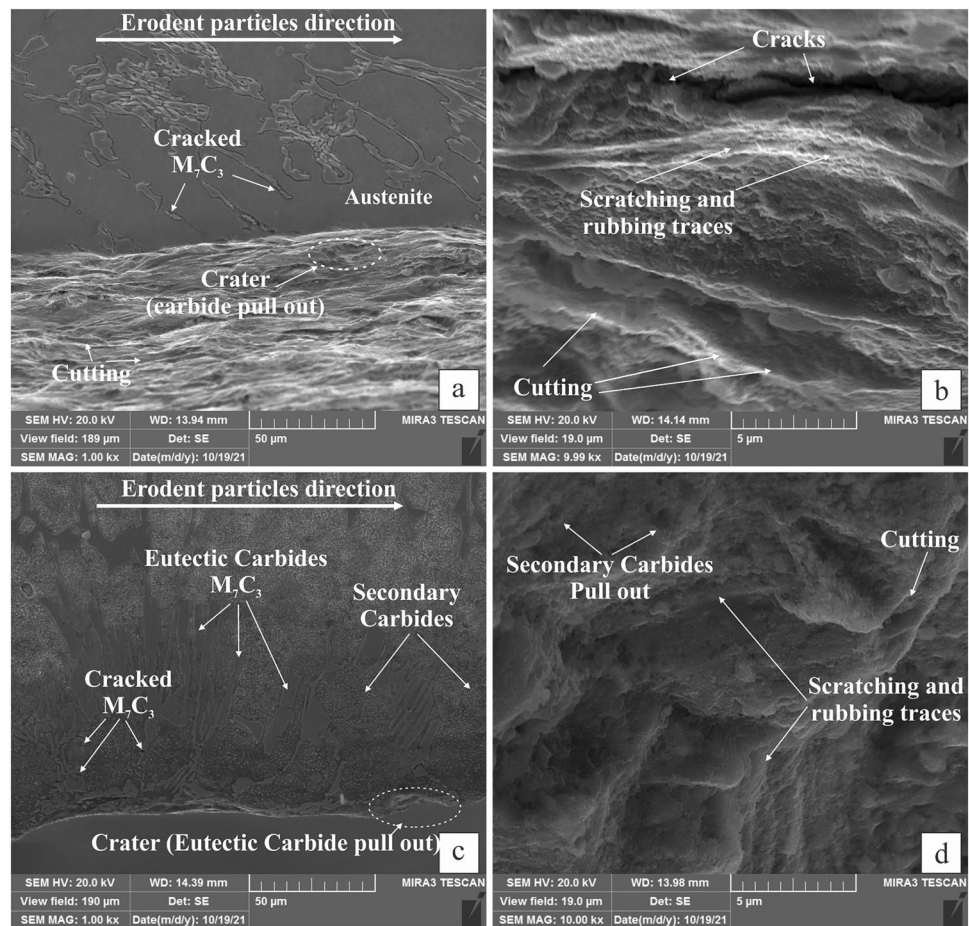
(Cr) − 15.2 by Maratray and Usseglio-Nanot [36], where % K represents the volume content of carbides. According to the above formula, the volume fractions of carbides in tested samples are 21% (HCCI-15) and 35.2% (HCCI-25).

3.2 Hardness Measurements

Table 4 shows the hardness values measured on both samples, in as-cast condition and after HT. On HT samples (HCCI-15-HT and HCCI-25-HT), the lower values of hardness are obtained.

3.3 Erosion Test Results

The elliptical shape of the eroded surface is noticeable on all 4 tested samples, as shown in Fig. 5. The ranges of obtained radii are 100–110 mm (longer one) and 80–90 mm (shorter one).

The area affected by erosion makes up approximately 45–50% of the total area on each sample. A similar shape of the eroded zone with the observable plastic deformation, up to varying degree, by the marked direction of the erodent flow, could be observed on the surface of all tested samples. Such removals of material in eroded zones are a consequence of high impact energy of erodent particles (particle velocity of 90 m/s and feed particle rate of 3000 g/min). Also, observed uneven surface features in eroded zone correspond to subsurface defects in cast material and due to the uneven distribution of the hard phases in the local microstructure.

The obtained results for the mass loss, as indicators of erosion resistance of the tested materials in as-cast and HT conditions, are shown in Fig. 6. It can be concluded that the erosion resistance of as-cast samples (HCCI-15 and HCCI-25) is very similar and does not indicate the difference in volume fraction of carbides phase due to different chromium content. The similar mass losses for both samples are due to the presence of a soft austenitic matrix, regardless of the amount of hard primary carbide phase. The mass loss results for both alloys after HT, in comparison with the as-cast condition, indicate a slight increase in erosion resistance of HCCI-15-HT, but a more significant increase in erosion resistance for the HCCI-25-HT alloy. With the transformation of austenite into martensite within the matrix due to HT, the erosion resistance increase. The effects of this transformation on the erosion resistance increase are minor,
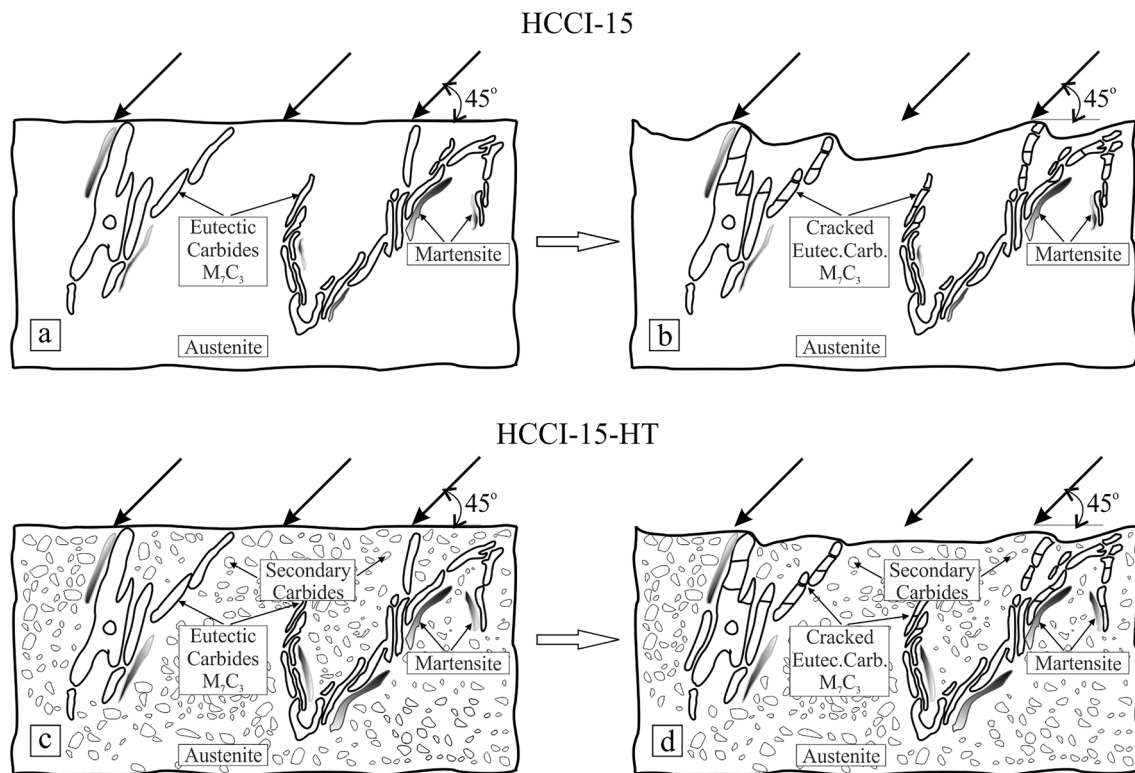
HCCI-15

HCCI-15-HT

Fig. 8 Schematic display of erosion mechanism in HCCI-15 alloys, as-cast and HT, before (**a**, **c**) and after erosion test (**b**, **d**)

compared to the contribution of the total volume fraction of the carbide phase in a matrix. The higher total volume fraction of carbides, and particularly of larger primary eutectic rod-shaped type M_7C_3 carbides in the HCCI-25-HT sample, additionally contributes to the increase in erosion resistance, as shown in Fig. 6.

3.4 Erosion Mechanisms

Erosion of both HCCI-15 and HCCI-15-HT alloys takes place by several different erosion mechanisms (Fig. 7a–d). The matrix of both materials is mainly eroded by the mechanism of cutting, scratching, and rubbing with significant plastic deformation. Eutectic carbides (M_7C_3), which are harder than the matrix, are eroded by the scratching mechanism, followed by carbides cracking and their microdefragmentation. During the erosion process, after significant erosion of the soft mainly austenitic matrix, also the pull-out mechanism appears and eutectic carbides are undermined and pulled out from the matrix.

Subsurface cracking of the rods-like shaped eutectic carbides appear, due to high energy collisions between matrix and erodent in both HCCI-15 samples, as shown in Fig. 7a, c. An additional mechanism of erosion of the HCCI-15-HT sample is the pulling out of secondary carbides from the matrix, as presented in Fig. 7d. Secondary

carbides distributed within the matrix of the HCCI-15-HT sample represent an obstacle to the collision between the material and erodent particles.

During the collision of erodent particles and secondary carbides in the matrix, the erodent particles change their directions, reduce their impact energy and speed, and thus decrease metal loss. Nevertheless, the contribution of secondary carbides to erosion resistance and decrease in mass loss is minor during severe erosion conditions of the HCCI-15-HT alloy, as shown in Fig. 6. In this case, the main contribution of secondary carbides is in the lowering of the plastic deformation of the matrix. It can be concluded that similar erosion mechanisms are operative for both tested samples (HCCI-15 and HCCI-15-HT). However, the higher plastic deformation of the matrix occurs in the as-cast sample with the softer matrix. Figure 8 schematically shows erosion mechanisms for HCCI-15 alloys, as-cast and after HT.

In both eroded HCCI-25 and HCCI-25-HT samples, as shown in Fig. 9a–d, similar erosion mechanisms are operative as in HCCI-15 alloy, i.e., cutting, scratching, and rubbing, as well as plastic deformation, microdefragmentation, and pull out of eutectic carbides. In the case of the HCCI-25 sample (Fig. 9b), the formation of lips due to plastic deformation is also observed. The higher volume fraction of eutectic rod-shaped and globular-shaped carbides, together with the matrix which contains uniformly distributed large

Fig. 9 SEM micrographs of eroded surface morphology HCCI-25 alloys: as-cast (**a**, **b**) and after HT (**c**, **d**)
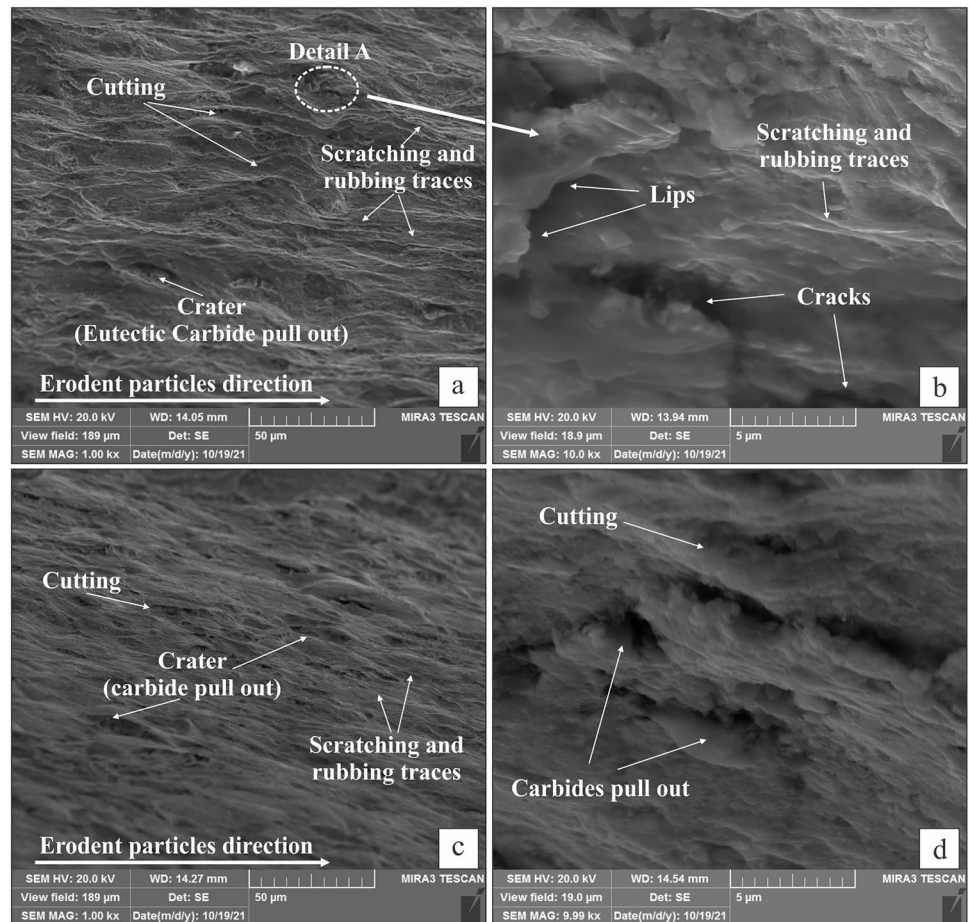
primary and fine secondary carbides, represents more efficient obstacles for erosion collisions. A larger number of collisions between the erodent particles and carbides lead to the reduction of the metal loss, as shown in Fig. 6.

It can be concluded that the erosion mechanisms in both tested alloys (HCCI-15 and HCCI-25) are similar. Both HT specimens (HCCI-15-HT and HCCI-25-HT) have better erosion resistance, compared to as-cast specimens, as shown in Fig. 6. The HCCI-25-HT sample has been found to be most erosion resistant due to the higher total volume fraction of carbides, particularly primary carbides in the matrix which are also larger, despite of slightly smaller volume fraction of secondary carbides in comparison with the HCCI-15-HT sample (see Figs. 3d and 4d). Figure 10 schematically shows erosion mechanisms for HCCI-25 alloys, as-cast and after HT.

4 Conclusions

In this study, the erosion behavior of two HCCI alloys with different chromium content (HCCI-15 and HCCI-25) was investigated. Both alloys were tested in as-cast and HT conditions. The conclusions are as follows:

- Both as-cast sample matrices (HCCI-15 and HCCI-25) were eroded by very similar erosion mechanisms, i.e., cutting, scratching, and rubbing with significant plastic deformation on the surface. On the as-cast HCCI-25 sample, in addition to the abovementioned mechanisms, the lips formation in the matrix is identified.
- Heat-treated samples (HCCI-15-HT and HCCI-25-HT) were also eroded by similar erosion mechanisms while the plastic deformation is less pronounced than in the case of as-cast samples. The presence of primary and secondary carbides in the matrix of heat-treated samples represents an additional barrier to erodent particles and increases the erosion resistance of both HT alloys.
- The eutectic M_7C_3 carbides in both alloys and both conditions are eroded by the mechanism of scratching and rubbing, followed by subsurface cracking and microdefragmentation. During the erosion of the matrix, the eutectic carbides are cracked, undermined, and pulled out from the matrix.
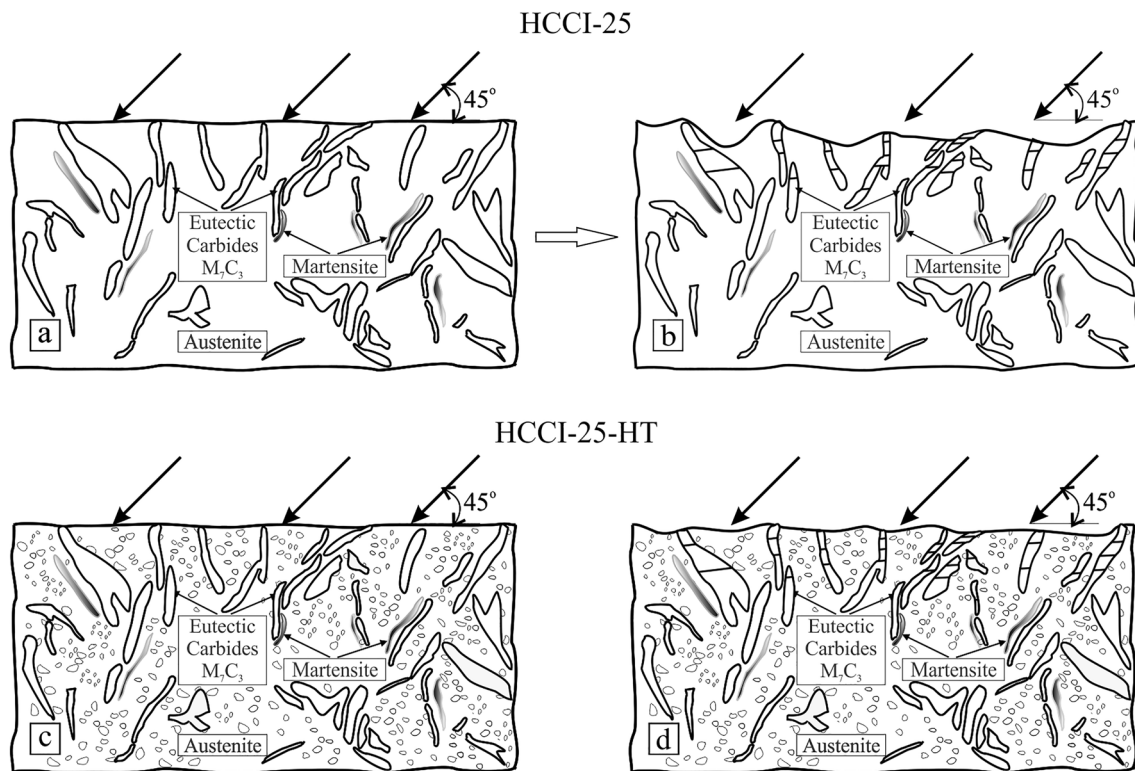
HCCI-25

HCCI-25-HT

Fig. 10 Schematic display of erosion mechanism in HCCI-25 alloys, as-cast and HT, before (**a**, **c**) and after erosion test (**b**, **d**)

- The primary and secondary carbide phase content in both HT alloys has the most significant effect on the increase of erosion resistance. Hence, the HCCI-25-HT sample shows the best erosion resistance due to a noticeably higher density of the primary carbides in the matrix which are also larger.

References

1. Raask E, Tube erosion by ash impaction. *Wear* **13** (1969) 301. https://doi.org/10.1016/0043-1648(69)90252-X

2. Maslarevic A, Bakic G M, Djukic M B, Rajicic B, Maksimovic V, and Pavkov V, *Trans. Indian Inst. Met.* **73** (2020) 259. https://doi.org/10.1007/s12666-019-01831-9

3. Abd El-Aziz Kh, Zohdy Kh, Saber D, and Sallam H E M, *J. Bio. Tribo. Corros.* **1** (2015) 1. https://doi.org/10.1007/s40735-015-0026-8

4. Zumelzu E, Goyos I, Cabezas C, Opitz O, and Parada A, *J. Mater. Process. Technol.* **128** (2002) 250. https://doi.org/10.1016/S0924-0136(02)00458-2

5. Chen L, Zhou J, Bushlya V, and Stahl J-E, *Proc. CIRP* **31** (2015) 172. https://doi.org/10.1016/j.procir.2015.03.092

6. Fortini A, Suman A, Zanini N, and Cruciani G, *Coatings* **12** (2002) 1218. https://doi.org/10.3390/coatings12081218

7. Lu F, Wei S, Xu L, Zhou Y, Wang X, Wang F, and Yi X, *Tribol. T.* **63** (2020) 325. https://doi.org/10.1080/10402004.2019.1690082

8. Zhou S, Shen Y, Zhang H, and Chen D, *Chin. J. Mech. Eng.* **28** (2015) 140. https://doi.org/10.3901/CJME.2014.0620.116

9. Hutchings I M, *J. Phys. D: Appl. Phys.* **25** (1992) A212. https://doi.org/10.1088/0022-3727/25/1A/033

10. Evans AG, in *Treatise on Materials Science and Technology*, (ed) Preece C M, *Materials Erosion* **16**, Academic Press, New York (1979) p.1.

11. Nguyen Q B, Nguyen V B, Lim C Y H, Trinh Q T, Sankaranarayanan S, Zhang Y W, and Gupta M, *Wear* **321** (2014) 87. https://doi.org/10.1016/j.wear.2014.10.010

12. Andrews D R, and Field J E, *J. Phys. D: Appl. Phys.* **15** (1982) 2357. https://doi.org/10.1016/0042-207X(85)90539-1

13. Al-Bukhaiti M A, Ahmed S M, Badran F M F, and Emara K M, *Wear* **262** (2007) 1187. https://doi.org/10.1016/j.wear.2006.11.018

14. Sundararajan G, and Roy M, *Tribol. Int.* **30** (1997) 339. https://doi.org/10.1016/S0301-679X(96)00064-3

15. Bousser E, Martinu L, and Klemberg-Sapieha J E, *J. Mater. Sci.* **48** (2013) 5543. https://doi.org/10.1007/s10853-013-7349-y

16. Oka Y I, Ohnogi H, Hosokawa T, and Matsumura M, The impact angle dependence of erosion damage caused by solid particle impact. *Wear* **203–204** (1997) 573. https://doi.org/10.1016/S0043-1648(96)07430-3

17. Karantzalis A E, Lekatou A, and Mavros H, *Int. J. Cast Met. Ras.* **22** (2009) 448. https://doi.org/10.1179/174313309X436637

18. Doğan Ö, Laird G I I, and Hawk J A, *Wear* **181–183** (1995) 342. https://doi.org/10.1016/0043-1648(95)90041-1

19. Karantzalis A E, Lekatou A, and Mavros H, *ASM Int. J. Mat. Eng. Perform.* **18** (2009) 174. https://doi.org/10.1007/s11665-008-9285-6

20. Sallam H E M, Abd El-Aziz Kh, Abd El-Raouf H, and Elbanna E M, *Mater. Des.* **52** (2013) 974. https://doi.org/10.1016/j.matdes.2013.06.045

21. ASTM G76, *Standard Test Method for Conducting Erosion Tests by Solid Particle Impingement Using Gas Jets*, ASTM International, 100 Barr Harbor Drive, PO Box C700, West Conshohocken, PA 19428–2959, United States.

22. Sijacki Zeravcic V, Bakic G, Djukic M, Rajicic B and Andjelic B, Parts I and II. Technical Report No 12-04a-12.04/2009, Faculty of Mechanical Engineering, University of Belgrade (2009)

23. Maslarević A, Bakić G M, Đukić M B, Rajičić B, and Maksimović V, Characterization of a coating 316l applied by plasma transferred arc. *Hem. Ind.* **73** (2018) 139. https://doi.org/10.2298/HEMIND170928005M

24. Dallaire S, *J. Therm. Spray. Techn.* **10** (2001) 511. https://doi.org/10.1361/105996301770349295

25. Cernuschi F, Guardamanga C, Capelli S, Lorenzoni L, Mack D E, and Moscatelli A, *Wear* **348–349** (2016) 43. https://doi.org/10.1016/j.wear.2015.10.021

26. Vieira R E, Mansouri A, McLaury B S, and Shirazi S A, *Powder Technol.* **288** (2016) 339. https://doi.org/10.1016/j.powtec.2015.11.028

27. Peat T, Galloway A, Toumpis A, Harvey D, and Yang W H, *Surf. Coat. Tech.* **300** (2016) 118. https://doi.org/10.1016/j.surfcoat.2016.05.039

28. Ruff A W, and Ives L K, Measurement of solid particle velocity in erosive wear. *Wear* **35** (1975) 195. https://doi.org/10.1016/0043-1648(75)90154-4

29. Lu L, Hiroshi S, and McLean A, *Mater. Sci. Eng. A* **347** (2003) 214. https://doi.org/10.1016/S0921-5093(02)00588-9

30. Li P, Yang Y, Shen D, Gong M, Tian C, and Tong W, *J. Mater Res. Technol.* **9** (2020) 5735. https://doi.org/10.1016/j.jmrt.2020.03.098

31. Bedolla-Jacuinde A, Hernández B, and Béjar-Gómez L, *Int. J. Mater. Res.* **96** (2005) 1380.

32. Doğan Ö, Hawk J A, and Laird G I I, *Metall. Mater. Trans. A* **28A** (1997) 1315. https://doi.org/10.1007/s11661-997-0267-3

33. Powell G L F, and Laird G I I, *J. Mater. Sci.* **27** (1992) 29. https://doi.org/10.1007/BF00553833

34. Tabrett C P, Sare I R, and Ghomashchi M R, *Int. Mater. Rev.* **41** (1996) 59. https://doi.org/10.1179/imr.1996.41.2.59

35. Gasan H, and Erturk F, *Metall. Mater. Trans. A* **44A** (2013) 4993. https://doi.org/10.1007/s11661-013-1851-3

36. Maratray F, and Usseglio-Nanot R, *Atlas-transformation characteristics of chromium and chromium-molybdenum white iron*, Climax Molybdenum S.A, Paris (1971).